Initial contact and spreading of a non-Newtonian drop on a solid surface

Hao Li, Qindan Zhang, Xiaofeng Jiang, Charly Koenig, Huai Z Li

Colloids and Surfaces A: Physicochemical and Engineering Aspects xxx (xxxx) 133066

Contents lists available at ScienceDirect

Colloids and Surfaces A: Physicochemical and Engineering Aspects

journal homepage: www.elsevier.com/locate/colsurfa

Initial contact and spreading of a non-Newtonian drop on a solid surface

Hao Li [a], Qindan Zhang [a, b], Xiaofeng Jiang [a, c], Charly Koenig [a], Huai Z. Li [a, *]

[a] Laboratory of Reactions and Process Engineering, CNRS, University of Lorraine, 1, Rue Grandville, BP 20451, 54001 Nancy Cedex, France
[b] Institute for Systems Rheology, School of Mechanical and Electrical Engineering, Guangzhou University, Guangzhou 510006, China
[c] School of Chemical Engineering and Technology, China University of Mining and Technology, Xuzhou 221116, China

ARTICLE INFO

Keywords:
Drop spreading
Drop containing nanoparticles
Fast spreading
Small spatiotemporary scale
Micro-PIV
Scaling laws

ABSTRACT

In this work, the very initial contact and spreading of drops of two non-Newtonian fluids on a hydrophilic stainless-steel surface were comparatively investigated. The fluids employed were respectively a polymer solution of polyacrylamide (PAAm) and an aqua dispersion of fine graphene oxide (GO) particles. Experimental studies involved visualizing and characterizing the spreading width over time on the substrate surface. A more precise investigation into the initial contact and spreading of non-Newtonian pendant drops on a solid surface was performed through a home-made ultra-high-speed direct current (DC) electrical device with an acquisition frequency up to 1.25 MHz (time interval of 0.8 μs), a high-speed camera and a home-developed high-speed micro-particle image velocimetry (micro-PIV). The competing mechanisms of related forces: inertial, viscous, and capillary forces were probed to lead to different scaling laws.

1. Introduction

Liquid wetting and spreading on solid surfaces have been extensively studied because of its common existence in our daily life, as well as in numerous industrial applications such as inkjet printing, spray coating, raindrop splashing on the windshield, and pesticide spraying, etc. [1–4]. From a fundamental point of view, the wetting and spreading dynamics of liquid drops on solid surfaces have been described as follows: a microscopic precursor film propagates ahead of the drop, subsequently the interfacial force drives drop spreading, a final equilibrium would be reached in the end [5]. The understanding of this complex dynamics involving gas-liquid-solid phases, especially at the initial stage, becomes then essential [6].

Parameters affecting the initial contact and spreading include the properties of fluids [7,8], such as viscosity, density, surface tension, elasticity, etc., and substrate surface conditions [9,10], including material, roughness and wettability [11–14], etc. Experimental approach often involves visualizing and characterizing the spreading width over time on the substrate surface.

A common investigation concerns usually drop wetting and spreading on a smooth solid surface. In particular, the spreading at its very initial stage is mainly dominated by inertia forces, then followed by viscous force [15]. Further comparison between these two stages is made through the drop contacting width [16,17]. Spreading on partially wetting surfaces such as hydrophobic surfaces for aqueous drops, on the other hand, is usually part of drop impact process [18]. For the very initial spreading with a short time interval, the wettability of the solid substrate is considered irrelevant to spreading dynamics [19]. In fact, the initial spreading depends mainly on the surface tension between the drop and the surrounding fluid. Afterwards, the subsequent spreading displays a complex feature of triple line contact between the drop, the solid substrate and the surrounding air.

Existing works [15,20] reveal that the spreading width vs. time follows the form of a power law $W \sim t^{\alpha}$. Different values of α also indicate various dominant forces involved in the spreading dynamics under different regimes. Three distinct regimes were mainly scaled respectively: inertial regime, capillary regime, and inertia-capillary regime [13,21]. For fluids with lower viscosities, the drop spreading width W grows exponentially with time t with an exponent $\alpha = 0.5$ in the inertial regime [15]; on the other hand, for high-viscosity drops, viscous force dominates the spreading with $\alpha = 0.8$ initially to 0.1 at final equilibrium stages [19]. Chen et al. [12] studied the initial spreading of drops on viscoelastic rubber films confirming that early spreading is jointly dominated by inertia and wetting dynamics is dominated by wettability instead of softness. A similar scaling law was derived with exponent ranging from 0.2 to 0.5. Mitra et al. [21] investigated the drop spreading on a substrate surrounded by water and air. A transition of different stages was observed, which always began from an initial viscous regime with $W \sim t$, transiting to an intermediate inertial regime with $W \sim t^{0.5}$ and a final Tanner's regime with $W \sim t^{0.1}$. These regimes are typically mani-

* Corresponding author.
E-mail address: Huai-Zhi.Li@univ-lorraine.fr (H.Z. Li).

https://doi.org/10.1016/j.colsurfa.2023.133066
Received 13 October 2023; Received in revised form 7 December 2023; Accepted 21 December 2023
0927-7757/

fested if the variable spreading width is much smaller than drop size. Otherwise, a succinct power law is no longer valid [22–24]. For a total wetting spreading dynamics, the long-time behavior often follows the Tanner's law [16,25], where $W \sim t^{0.1}$. For partial wettings, deviations might occur at this stage.

For the initial spreading, the existing works have included many kinds of fluids, mostly Newtonian fluids, to name a few, water, glycerol, silicone oil, and mercury [9,26,27], etc. Non-Newtonian fluids, on the other hand, were much less reported [9,12,28–31]. To our best knowledge, the spreading dynamics of compound drops issued from solid-liquid dispersions is extremely rare in the literature. Recently, Fardin et al. [6] and Du et al. [9] showed that the coalescence, spreading, and pinch-off of drops are qualitatively similar on the basis of the Ohnesorge number for viscous non-Newtonian fluids: $Oh = \eta/\sqrt{\rho\sigma D}$ gathering the effect of viscosity, surface tension, density and drop size. Especially in polymer solutions, the fluid relaxation time along with *Oh* could distinguish the coalescence, spreading, and capillary breakup phenomena from Newtonian behavior. Graphene oxide (GO) dispersion [32,33] was studied extensively focusing mainly on its manufacture, application in the fields of drug delivery, cellular imaging, etc., through its electrical conductivity. Its dynamical behavior in the field of multiphase flows, however, was much less known. Given the critical character of such material in inkjet-printing process for highly flexible electronic devices [34,35], it is thus intriguing to further understand more within above-mentioned fields. From a practical point of view, the coating by a paint which is also a solid-liquid dispersion on a solid surface requires some peculiar knowledge compared to a homogenous liquid. To some extent, the GO dispersion could act as a model solid-liquid dispersion for real fluids such as paints and inks. The drop spreading investigation is then specially interesting for non-Newtonian fluids having similar shear-thinning behavior but displaying different structural property between a homogeneous polymer solution and solid-liquid GO dispersion.

The high-speed imaging method is expected to provide picturesque data and insights into analysis and validation of conceptual models and applications. Experimental techniques such as high-speed visualization with a side view or side and bottom view were adopted in the investigation of drop spreading [19,25], but visualization was largely limited by capturing frequency around 0.1 MHz with a satisfying spatial resolution, which is still far from sufficient for the fast spreading dynamics at the very initial stage.

Here, a more rapid approach into was developed in this work through a home-made ultra-high-speed DC electrical device [36] with an acquisition frequency up to 1.25 MHz (time interval of 0.8 μs) to monitor the initial contact and spreading of non-Newtonian pendant drops on a solid surface, along with a high-speed camera and a home-developed high-speed micro-PIV. In comparison to the conventional visualization, this newly developed DC technique allows to reduce a decade of time scale for the initial contact period between the drop and a flat solid surface.

2. Materials and methods

Fig. 1(a) shows the schematic diagram of the experimental setup. A stainless-steel nozzle with inner diameter of 0.6 mm and outer diameter of 0.97 mm was used to generate pendant drops in ambient air by means of precise syringe pump (PHD 2000, Harvard Apparatus, USA). The flowrates range from 0.01, 0.05 to 0.1 mL·min^{-1}, corresponding to approaching velocities of 0.06, 0.17 to 0.29 mm·s^{-1} towards the planar solid surface. Flowrates were varied to study the effect of approaching velocities on the initial spreading. A plate of stainless-steel with a diameter of 4 cm and thickness of 0.4 cm was horizontally placed under the nozzle's perpendicular position. The stainless-steel plate was firstly processed with a sander-polisher using a stiff cloth polishing wheel and pre-polishing paste in the mechanical workshop of our laboratory. Then, a soft polishing wheel and polishing paste were employed to refine better the surface. The maximum surface roughness within 1 μm for the plate was examined by both a scanning electron microscope (SEM, JSM-6490LV, JEOL, Japan) and an atomic force microscopy (AFM, MFF3D, Oxford Instruments, UK) around the drop contact zone, as shown in Fig. 1(b) and Fig. 1(c). Three additional measurements were repeated on the neighboring area to the contact zone to ensure the similar roughness. The DC electrical voltage *U(t)* between the drop-solid surface connection was recorded using a home-made ultra-high-speed acquisition device at a frequency of 1.25×10^6 Hz, as employed and detailly described in our previous study [36]. Electrodes were connected to the nozzle and the plate with the drop serving as conductive parts in the circuit. To visualize the contact and spreading evolution, images were captured from side view with a high-speed camera (Phantom V711, Vision Research, USA) with a macro lens (EF 100 mm f/2.8, Canon, Japan). The capturing speed is set at 84,054 frames per second (fps) restrained by drop contour and image resolution (max. 240 × 240 pixels at 84,054 fps). MATLAB (R2019b, MathWorks, USA) was used to analyze voltage and image data through programmed algorithms. Strict control of vertical distance between the nozzle and metal surface was conducted through our experiments. Such distance is small enough that the occurrence of contact took place before neck thinning and neck width at the nozzle outlet keeps constant during the very initial contact, which is called "contact before necking".

A high-speed micro-PIV technique was modified and then employed to probe the flow fields in the fluid during the spreading process. Sufficient amount of silver-coated hollow glass spheres (S-HGS-10, Dantec Dynamics, Denmark) with an average diameter of 10 μm were firstly uniformly dispersed in the aqueous non-Newtonian liquids as seeding particles. Unlike pulsed lasers with two cavities in the classical PIV or micro-techniques as used in our group, two continuous laser beams (LaserMax Inc., USA) of 1 mW were placed in horizontally-opposite directions to excite seeding particles inside the pendant drop. Formerly mentioned high-speed camera were used to captured images at a frequency of 5000 fps. The flow fields were computed using such images with the help of commercial software DynamicStudio (Dantec Dynamics, Denmark). It is worth noting that currently, pulsed laser sheets exceed difficultly 1000 pulses/s with two cavities, the combination of continuous laser beams with a high-speed camera is then the suitable and still difficult way to monitor the initial velocity fields at short time scale.

Two non-Newtonian fluids: 1.25 wt% polyacrylamide (PAAm, SNF Floerger, France) of molecular weight 1.3×10^7 g·mol^{-1} with 5 wt% NaCl solution and 4 mg/mL Graphene Oxide/GO dispersion (Graphenea, Inc., Spain) were used. Graphene Oxide dispersion that we used is a water-based dispersion of fine graphene oxide particles (size range: D_{90} 5–7 μm; D_{50} 2–4 μm; D_{10} 1–2 μm), which is prepared by hypersonification to obtain a homogeneous buoyant suspension afore experiments. The electrical conductivity of polymer solution and graphene oxide dispersion is 97.7 and 3.87 mS·cm^{-1} (22.8 °C), respectively.

NaCl was added into the PAAm solution for the purpose either to enhance the liquid electrical conductivity or to adjust its rheological behavior compared to that of GO dispersion. Certainly, the adding of salt into the solution of polymers would cause degradation of rheological properties or surface tension. The amount of NaCl to be added into the PAAm solution was carefully adjusted to meet the similar rheological properties of the GO dispersion used. Fig. 2 compares the rheological properties of these two shear-thinning non-Newtonian liquids measured in a cone-plan geometry on a rheometer (AR-G2, TA Instruments, USA), which includes the property of original polymer solutions' without adding of salt as well to illustrate the salt effect on the viscosity in the 1.25% PAAm solution.

As shown in Fig. 2(a), the GO that we used at its 0.4 wt% concentration exhibits shear-thinning behavior within the same shear rate range

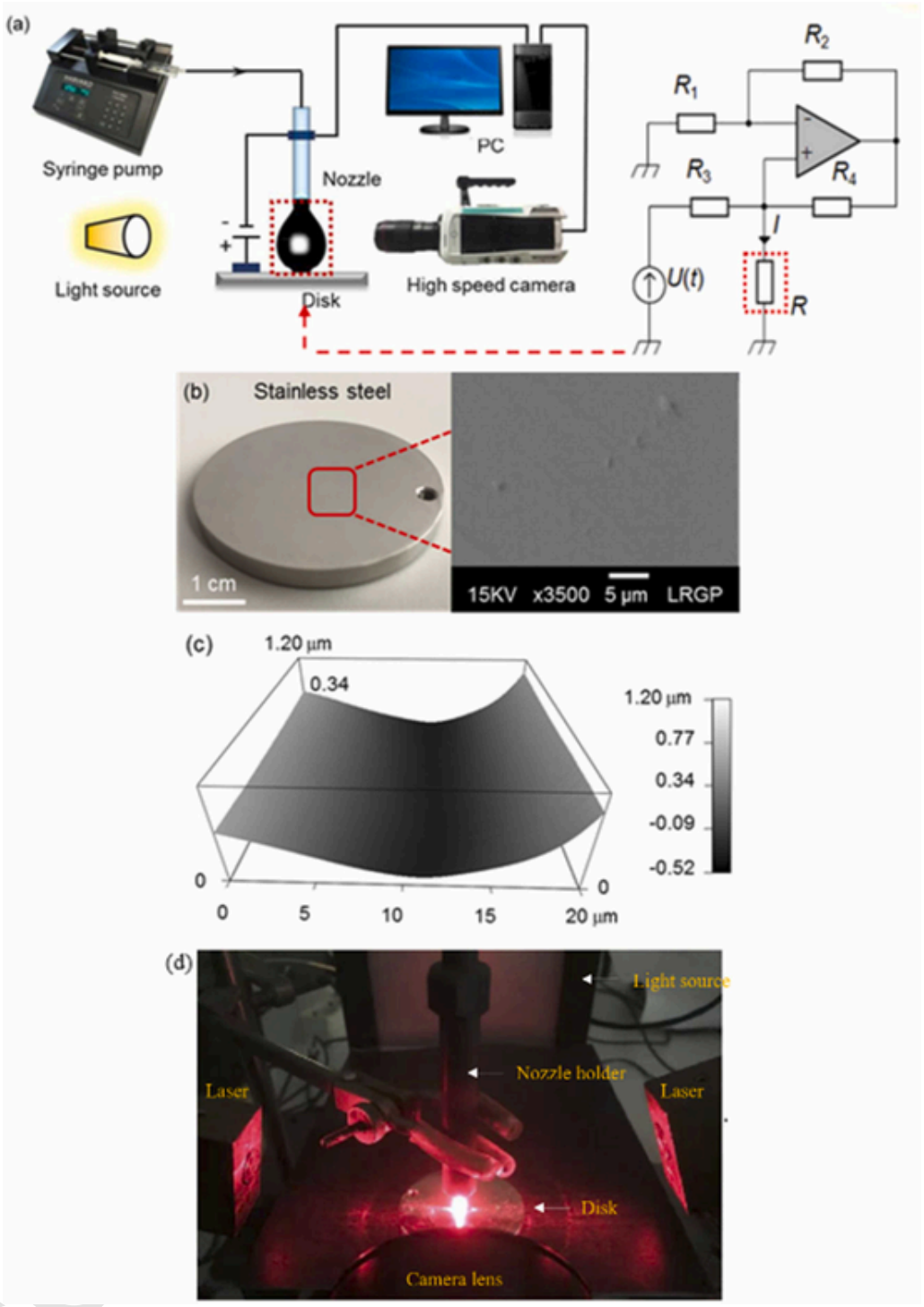

Fig. 1. (a) Schematic of the experimental setup. (b) SEM image for the surface of the stainless-steel plate. (c) AFM result for the surface of the stainless-steel plate. (d) Photograph of the working micro-PIV set.

of PAAm fluids. Obviously, the rheological behavior is quite similar between them except at very low shear rates.

For a polymer solutions like PAAm, the external shear could originate alignment and orientation at macromolecular order. When GO particles are dispersed in a liquid, under similar shear stress, the nanoparticles can re-orient and self-organized leading to a shear-thinning behavior. In contrary, interactions between particles of higher sizes could induce more friction due to the space limitation then to shear-thickening effect.

GO dispersions can exhibit Newtonian or non-Newtonian rheological behavior under steady shear flow depending on the concentration. At very low concentrations, the shear viscosity of GO dispersions shows Newtonian behavior. With increasing concentrations, typical shear-thinning behavior becomes dominant, usually associated with the existence of re-orientation of the GO particles forming a so-called nematic phase [37–39].

The relationship between the viscosities obtained by studying the steady shear flow and the applied shear rate can be approximated using a power-law relationship [39]:

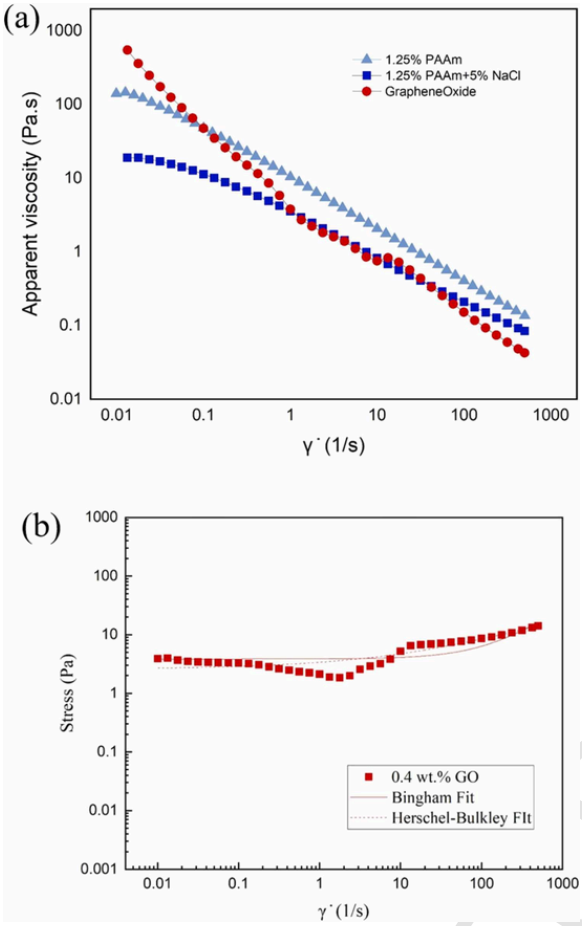

Fig. 2. (a) Comparison of the rheological properties between two non-Newtonian fluids. The salt effect was illustrated through 1.25% PAAm without salt. (b) The fit of the models to the steady shear flow data. (The solid lines show the fit of the Bingham model, and the dashed lines show the fit of the Herschel–Bulkley model).

$$\eta = K\dot{\gamma}^{n-1} \tag{1}$$

where η is the viscosity, K consistency, $\dot{\gamma}$ the shear rate and n power-law index [40]. An exponent with $n = 1$ corresponds to Newtonian behavior, whereas $n < 1$ is related to shear-thinning fluids. For low concentrations of GO, such as 0.08 wt%, n was ound to be 0.9 [39], which indicates a close behavior to Newtonian fluid. For higher concentrations, such as 1.8 wt%, n is found to be 0.29, which corresponds to weak gels. For the GO dispersions used in our work, the exponent n is found to be 0.41, which indicates a non-Newtonian shear-thinning behavior.

In addition to a power-law between shear viscosity and shear rates, to incorporate possible yield stress, further fitting of stress-shear rate data with Bingham and Herschel-Bulkley models were conducted [41], as shown in Fig. 2(b).

Bingham model:

$$\tau = \tau_0 + \eta_\infty \dot{\gamma} \tag{2}$$

Herschel-Bulkley model:

$$\tau = \tau_0 + K\dot{\gamma}^{n-1} \tag{3}$$

where τ is the shear stress, η_∞ is the infinite shear rate viscosity, τ_0 is the yield stress, K consistency and n exponent.

For Bingham model, the fitted yield stress $\tau_0 =$ 3.82 Pa, infinite shear rate viscosity $\eta_\infty =$ 0.025 mPa·s, $R^2 =$ 0.78. For the Herschel-Bulkley model fit, the exponent $n =$ 0.434 with $K =$ 0.79 Pa.s^n, $R^2 =$ 0.93, which indicates a better fit than the Bingham model.

As the GO dispersion is opaque due to the presence of GO particles, the transparent PAAm solution can then be considered as model fluid to allow the velocity measurements by the micro-PIV technique by means of the seeding particles. The initial contact takes place instantly when the drop contacts the plate and expands quickly in a very short time. The properties of the liquids used are listed in Table 1.

To validate the comparison between dimensionless numbers at close viscosities, we need to know that the targeted spreading dynamics is within our selected range of shear rate and corresponding shear viscosities. We consider shearing induced by spreading at horizontal direction, suggesting $V_0 = \partial W/\partial t$ and $D_0 =$ 2.9 mm. The shearing rate jumps to 200 s^{-1} - 1000 s^{-1} considering time-dependent shearing at first 4.28 × 10^{-4} s. For the convenience of calculation and comparison, we chose 0.0375 Pa·s for GO and 0.1082 Pa·s for PAAm as their apparent viscosity η_a, both determined at the shearing rate of 300 s^{-1}. In a review study of coalescence of drops, Kavehpour et al. [29] collected dimensionless time of coalescence using inertial and viscous timescale as a function of Ohnesorge number ($Oh = \eta_a/\sqrt{\rho D_{\max}\sigma}$) to identify proper timescale that should be used at different ranges of Oh. When $Oh \ll 1$, the effects of inertial forces contributed more to the resisting forces of spreading, which means inertial timescale $t_i = \sqrt{\rho D_{\max}^3/\sigma}$ is a more proper timescale; while for cases of $Oh \gg 1$, viscous timescale $t_\mu = \eta_a D_{max}/\sigma$ is more suitable.

Compared with data obtained in our experiment, viscous timescale t_μ should be used for analysis of spreading with $t_i \gg t_\mu$. In other words, if $Oh = t_\mu / t_i \ll 1$, combining with rheology data of Fig. 2, shearing rate needs to be larger than ~20 s^{-1} for both liquids, otherwise $t_\mu / t_i > 1$. Clearly, short time initial spreading of GO and PAAm drops fits the former case in our study. However, a specific range of $0.2 < Oh < 1$ where inertial and viscous forces both contributes to the resisting force in the spreading process is also mentioned. With $Oh_{PAAm} \approx 0.238$, it is also necessary to take a look at the data with viscous timescale.

Sequences for the initial contact and spreading of pendant drops at solid surface are illustrated in Fig. 3. The DC device and high-speed camera are synchronized with time zero $t_0 =$ 0 s, which is defined as the moment when the first decreasing point of electrical resistance is detected. The moment the drop touches and spreads spontaneously on the plate, the gas film between the drop and the metal surface is evacuated in a very short time to allow the electric signal monitoring. Within such a short period, the electric voltage drops drastically as the conducting liquid bridge connected the liquid with the steel. And capturing images at such short time and scale poses great challenges to obtain quantitative data with accuracy.

3. Results and discussion

According to Fig. 3, up till the images to $t =$ 0.50 ms, the spreading width keeps increasing while the drop contour remains unchanged. The voltage decreases gently compared to the very initial contact at the be-

Table 1
Properties of the liquids used.

Liquids	ρ (kg·m^{-3})	σ (mN·m^{-1})	η_a (Pa·s)	λ (mS·cm^{-1})	K	n_a	Oh	t_i/t_μ
1.25 wt% PAAm + 5 wt% NaCl	1066	67.7	0.1082	97.7	17.98	0.433	0.237	4.21
Graphene Oxide	1004	50.73	0.0375	3.87	48.08	0.530	0.097	10.25

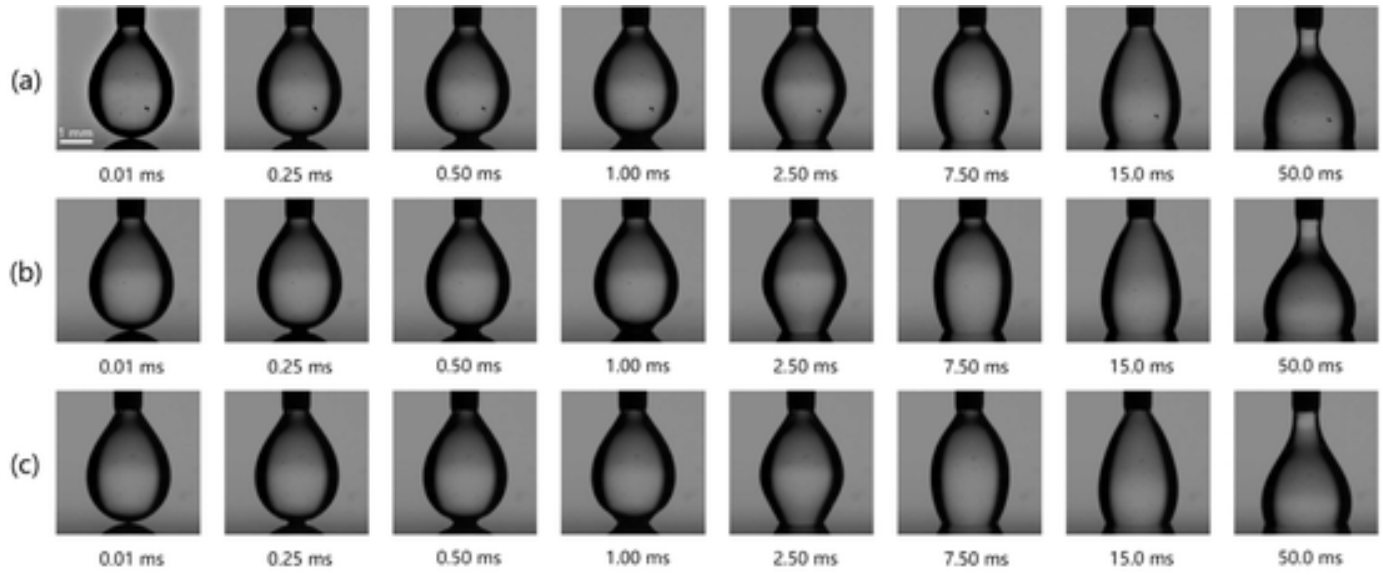

Fig. 3. Sequence for initial contact and spreading of a pendant drop of 1.25 wt% PAAm with 5 wt% NaCl on a stainless-steel surface. (a) 0.01 mL/min (b) 0.05 mL/min. (c) 0.1 mL/min. All images share the same scale bar of 1 mm.

ginning of this time period. Keeping a continuous liquid flowrate through the nozzle, the lower half of drop begins to take the shape of a trapezoid. At $t = 2.5$ ms, the drop is much like a bowling pin and the latitude of largest width still lies at the equatorial. At $t = 7.5$ ms, the drop becomes a quasi-cylinder and the voltage reaches a local extremum. Due to the continuous liquid feeding, the upper half of pendant drop starts to contract while the bottom part continues to expand and accumulate liquid on the surface. At $t = 15$ ms, the drop evolves quite like a pear and the voltage decreases into a local minimum. At around $t = 50$ ms and longer away, the drop deforms like a perfect conical flask. Thereafter, the upper part of pendant drop gradually thins into a neck. The neck pinch-off thins to be a liquid column from $t = 50$ ms and then detaches from the bottom bulk after the filament breaks up. The voltage increases continuously until the final pinch-off at $t = 1637.8$ ms. Due to the viscoelasticity of PAAm solutions, the drop neck would be elongated thus the whole period is much longer than water as well as carboxymethyl cellulose sodium (CMC) and Emkarox solutions as pointed out by the our previous work [36].

The electrical resistance R of initial contact is displayed in Fig. 4. The connective circuit is formed as soon as the pendant drop contacted the plate surface, and the resistance decreases rapidly due to the initial connection of the circuit. Our previous works indicates that in fluids such as salted water and polyethylene oxide (PEO) solutions, the magnitudes of resistance detected meet certain minimum values in a very short time[36]. However, in this case, the resistance never reaches minimum but exhibits a constant decreasing tendency.

The dynamics of initial contact and spreading from both electrical signals and images are illustrated in Fig. 5. The electric resistance depends on the minimum drop cross section along the falling drop where the motion of electrons is largely obstructed, either at the drop base or neck. The smaller the dominant width, the larger the drop resistance. At very early stage of initial contact (less than 0.01 ms), the spreading width at the scale of nanometer is much shorter than that of drop neck. The electrical signal is then dominated by the spreading width, due to the linear relationship of conductance with spreading width. The drop spreads quickly and the neck gradually begins to take effect. For 1.25 wt% PAAm with 5 wt% NaCl solution, the drop base increases to 0.94 mm at $t = 0.7$ ms and became adequate with the neck width as shown in Fig. 5. The drop base and neck contribute both to the resistance, the drop resistance reaches the minimum at this point. Then the drop base increases to larger than the neck width and the neck width became

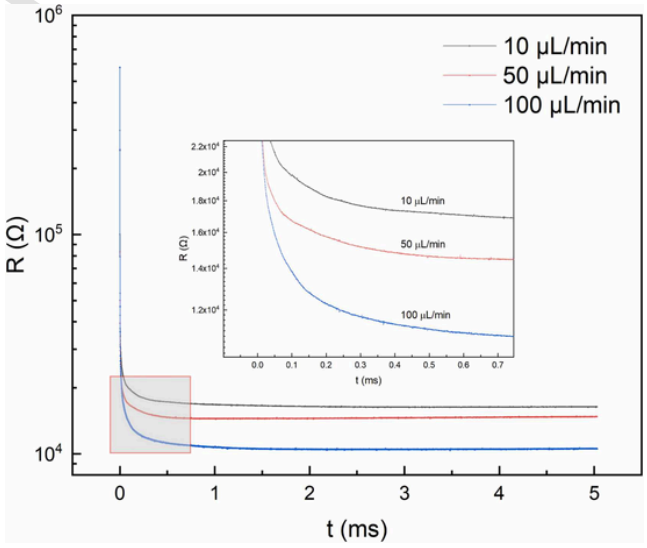

Fig. 4. Electrical signals of initial contact for 1.25 wt% PAAm with 5 wt% NaCl drops on a stainless-steel plate. The inset shows the scale up of the resistance drop within 0.7 ms. The injection speed of liquid was marked accordingly with 10, 50, 100 μl/min.

dominating. The neck gradually thins, and the resistance starts to increase until the final pinch-off of the drop, where the contribution of the drop base on the resistance is less than 0.01% and totally dominated by the neck width. The contribution of the drop base is inversely proportional to its width during the spreading process. In this work, we focus on the initial contact stage of drop before the drop conductance G reaches maximum about 1 ms.

The drop conductance G is the reverse of the resistance: $G = 1/R = \lambda \iint_S \boldsymbol{E} \bullet d\boldsymbol{S} / \int_A^B \boldsymbol{E} \cdot d\boldsymbol{l}$ that depends mainly on the minimum section of falling drop contacting with the planar surface where the motion of ions is largely obstructed. The algorithm is no longer valid after 4.8 μs as shown by the experimental curve for conductance, as shown in Fig. 5(b). This is because when the height between the nozzle and the planar surface is fixed, the dominant conductance G is in the contacting section as long as the width here is less than 2.5% of the liquid neck

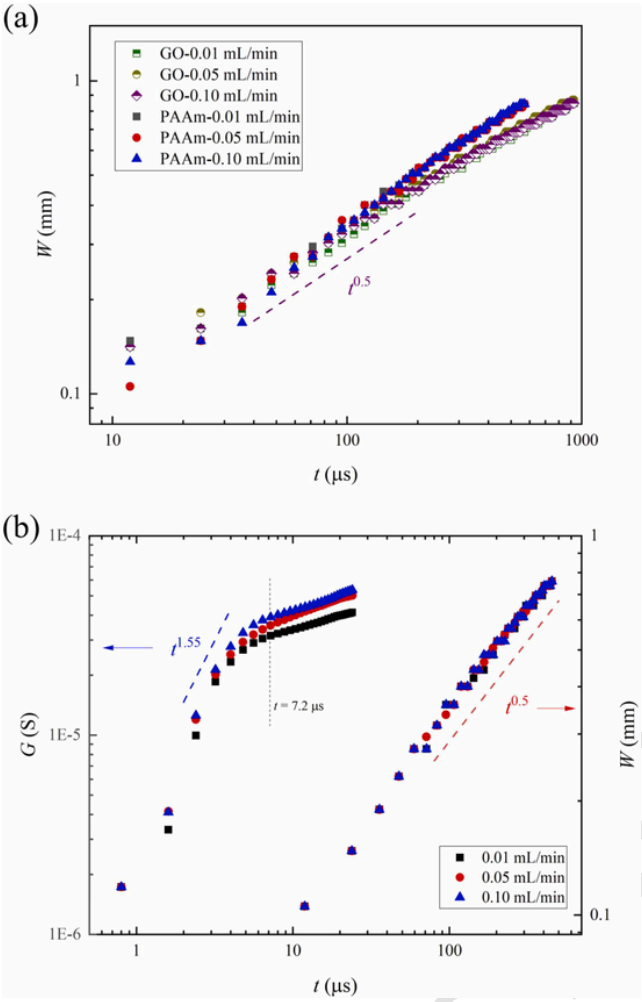

Fig. 5. (a) Variation of the PAAm drop coalescing width W with time t. (b) Variation of the PAAm drop conductance G versus time t and of the coalescing width W with time t. Dashed lines are drawn to guide the eyes.

width at the outlet of the nozzle. Hence, the coalescing width $W \sim G^{1/2}$ is invalid when $W \leq 95$ μm, spreading law should be experimentally corroborated by both the enlarging section and the drop shape evolution. The drop spreads, meanwhile the neck between the nozzle and the coalescing surface gradually takes charge of change of conductance.

In our experiments, the drop conductance follows a power-law of $G \sim t^{\alpha}$ with time during the initial contact and spreading, as illustrated in Fig. 5(b). At the beginning period that is measured by the electrical DC device, we have a power law with $\alpha = 1.55 \pm 0.21$ within 7.2 μs. This value is similar for both fluids and all approaching velocities, which indicates a fast spreading taking place with the liquid front advancing with aqueous solvent. Followed by another regime after 11.9 μs is the scaled results of $W \sim t^{\beta}$ from high-speed imaging results with exponents of $\beta = 0.54 \pm 0.01$. The difference could be explained with the help of micro-PIV velocity fields as presented in Fig. 6. All velocity data were calculated and modified with the help of commercial software DynamicStudio by eliminating irrelevant vectors. Some results from our previous studies are also included [36]. The dominant inertia could be seen stemming from the surface energy at the neck area.

However, this process is largely dampened by increased viscosities of fluids. The generation of capillary waves originated from the triple contact line between three phases and travels upwards along the drop surface. Its generation is induced by the release of surface energy. As soon as generated, it induces the deformation of drop curvature. This is easier to be seen with low-viscosity fluids like water and low viscosity carboxymethyl cellulose sodium (LV CMC). Du et al. [9] attribute this phenomenon to the dissipation of viscous forces and enhanced interfacial effect.

Obviously, the exponent value of β in the width evolution law $W \sim t^{\beta}$ for PAAm ($\beta_{PAAm} = 0.64$) is slightly higher than Graphene oxide dispersion ($\beta_{GO} = 0.52$), also at a later stage with $\beta_{PAAm} = 0.48$ and $\beta_{GO} = 0.42$. This could be explained by examining the viscosity difference of these two fluids. PAAm and GO are both shear-thinning non-Newtonian fluids. At reduced shear rates corresponding to slow drop spreading, the viscosity of the PAAm solution is lower than that of the GO solution as shown in Fig. 2. At later stages of spreading, the real Ohnesorge number based on the instantaneous fluid viscosity would be smaller for the PAAm solution, displaying then less viscous forces compared to the GO solution. Some researchers [9,15,19,26,28] have looked closely into the relationship between the exponent β and Oh considering different regimes of spreading process: inertial dominant regime and viscous dominant regime, regardless of some contrary results.

In order to correlate data from both electrical signals and high-speed images, we rescale $G \sim t^{\alpha}$ and $W \sim t^{\beta}$ into a dimensionless scaling $\Phi \sim \tau^{\omega}$ by considering $W \sim G^{1/2}$, and taking $\Phi = W/D_{max}$ and $\tau = t/t_i$, where D_{max} is the largest width of the drop at the starting moment of spreading and $t_i = \sqrt{\rho D_{\max}^3/\sigma}$ is the inertial time. Also, to overlap these data of different time ranges, we extended two data points at time $t = 6.4$ and 7.2 μs by approximating with $G \sim t^{1.55}$. The results are gathered and displayed in Fig. 7 between these two different fluids.

Similar tendency is observed for both the GO and PAAm solutions though they are two different fluids in many ways: one is a solid-liquid dispersion and another one homogeneous respectively. We could then consider the PAAm as transparent model fluid for the black GO and study its velocity fields inside a spreading drop by the micro-PIV technique. Generally, different Oh numbers would only take effect when itself is far bigger than unity, especially at phases entering Tanner's regime. With decreasing Oh, the exponent ω would increase from close to 0.3 to 0.5.

Four distinct regimes could be easily identified in Fig. 7, specifically, with $\omega = 0.75$ for the inertial limited viscous (ILV) regime, $\omega = 0.5$ for the inertial regime, an intermediate transition regime and $\omega = 0.1$ for the well-known Tanner's regime. Besides the classical inertial and Tanner's regimes, ILV regime is proved for the first time with the electrical signal experiments at very low time scale, which is marked separately from later optical data at dimensionless time point $\tau \approx 0.62$. A similar regime for coalescence processes between a drop and a planar liquid surface was formerly reported via the similar approach in our previous works [36]. The transition regime exhibits a non-monotonous transition from the inertial regime to the Tanner's regime. The standout exponents of rescaled spreading process indicate that once the liquid drop enters in contact with the solid, the electric conductance increases very rapidly. The change of scaling law is mainly due to the high conductivity of solutions which is a very sensitive monitoring parameter in our electrical DC device. Similarly, the drop spreading width follows a power law with time as $W \sim t^{\beta}$.

For both fluids, a close to 1/2 exponent at the inertial dominant regime implies a typical drop spreading process on a super-hydrophilic surface (contact angle close to 0°) [9]. As for final spreading regime of drops after $\tau = 1$, the exponents stabilized at $\omega = 0.10$ and 0.12, respectively for both the PAAm and GO. The value of the exponents is in good agreement with the Tanner's law. As shown in Fig. 7, the viscosity effect is not dominant for the initial spreading on a total wetting and smooth horizontal surface. Yet a close to 1/10 exponent at the final spreading also implies that capillary forces play an important role in an infinitesimally thin film as for Newtonian fluids [9]. Understanding the processes of liquid spreading in such a way, especially of complex non-Newtonian fluids including Graphene oxide fluids, would mostly likely help the refinement of applications such as in ink-jet printing, cosmetics, etc.

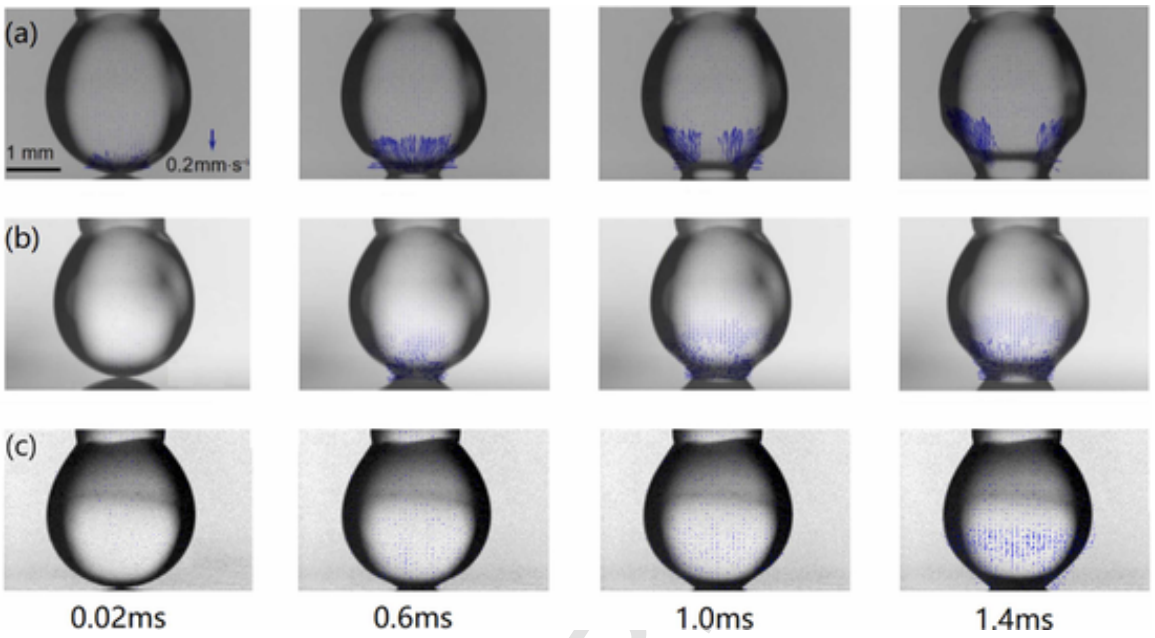

Fig. 6. Velocity fields in the drop during the initial contact and spreading of different fluids: (a) Water + 5 wt% NaCl solution at $v_0 = 0.29$ mm·s^{-1}, $Oh = 4.54 \times 10^{-3}$ at $t = 200$ μs; (b) 2% LV CMC + 5 wt% NaCl solution at $v_0 = 0.29$ mm·s^{-1}, $Oh = 0.77$ at $t = 200$ μs; (c) 1.25% PAAm + 5% NaCl, $v_0 = 0.29$ mm·s^{-1}, $Oh = 4.56$ at $t = 200$ μs. The scale bars for length and velocity represent 1 mm and 0.2 mm·s^{-1}, respectively, and stands for all figures.

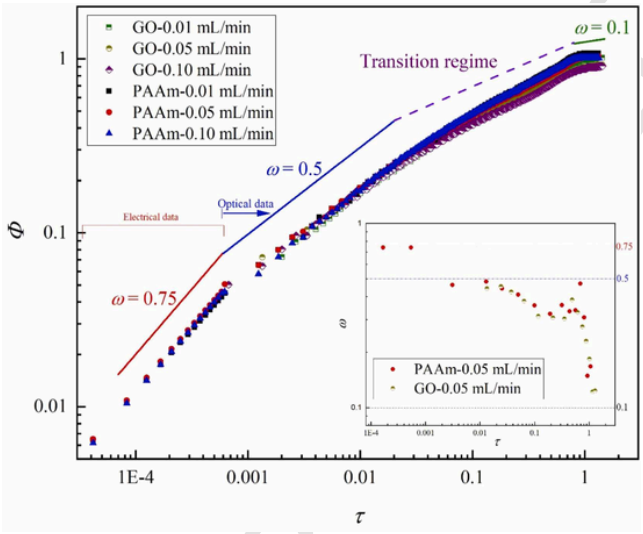

Fig. 7. Variation of the dimensionless spreading width Φ with the normalized time τ combining electrical and optical image data. Solid lines represent overall trends covering their span and also are used to guide the eyes.

4. Conclusion

In summary, the focus of the work is to study the spreading behavior of an opaque solid-liquid dispersion, to compare with homogenous polymer solution of similar rheological properties. and to validate finally the experimental approaches to expand both the spatial and time scale for very fast phenomena. In particular, the initial contact and spreading dynamics of compound drops on a planar solid surface were experimentally investigated through three different and complementary techniques. The evolution of the electrical conductance in close relation with the drop spreading width was firstly detected at the time scale from 0.8 μs to 10 μs. Two distinct fluids with similar rheological properties, GO and PAAm, were examined. Specifically, the results show that the conductance drop conductance in relation with the spreading width during the spreading follows a scaling law: $G \sim t^{1.55 \pm 0.21}$ within 7.2 μs for PAAm drops and the visualized width follows a scaling law of $W \sim t^{\beta}$ ($\beta_{PAAm} = 0.64$, $\beta_{GO} = 0.52$), also at a later stage with $\beta_{PAAm} = 0.48$ and $\beta_{GO} = 0.42$. Further dimensionless scaling $\Phi \sim \tau^{\omega}$ combining conductance and imaging data reveals four different regimes during the spreading with $\omega = 0.75$ for the inertial limited viscous (ILV) regime and $\omega = 0.5$ for the inertial regime. This rescaled power law represents well for both fluids at the initial spreading stage. After $\tau = 1$, the exponents stabilize around 0.1 and 0.12, respectively for PAAm and GO solutions. Viscosity effect is not dominant for initial spreading on a total wetting and smooth horizontal solid surface, despite different fluid types: nanoparticles dispersion vs. homogeneous fluid. The quantification of flow fields inside a spreading drop by considering the PAAm as a model fluid for GO was performed through the micro-PIV technique. The exponent would increase from close to 0.3 to 0.5 with decreasing *Oh*. As for the PAAm fluid, a close to half unity exponent at inertial dominant regime implies a typical drop spreading process on a super-hydrophilic surface. ILV regime is proved for the first time with electrical conductance experiments. Intermediate transition between typical inertial and Tanner's regimes proved to be non-monotonous for both fluids. The results could add new bricks for better understanding the spreading for drop before 0.01 ms beyond the usual scope of high-speed camera. Hopefully, further studies involve opaque fluids like GO dispersion are expected to examine the effect of their nature on the spreading dynamics at both very short time scale and low spatial scale with the help of the current approach. The insight gained in this study could help our further modeling and simulation by means of Lattice Boltzmann (LB) method.

CRediT authorship contribution statement

Li Huai Z: Conceptualization, Data curation, Formal analysis, Funding acquisition, Investigation, Methodology, Project administration, Supervision, Validation, Writing – original draft, Writing – review & editing. **Koenig Charly:** Data curation, Methodology. **Jiang Xiaofeng:** Data curation, Formal analysis, Investigation, Visualization. **Zhang Qindan:** Data curation, Investigation, Methodology, Visualization. **Li Hao:** Data curation, Formal analysis, Investigation, Methodol-

ogy, Validation, Visualization, Writing – original draft, Writing – review & editing.

Declaration of Competing Interest

The authors declare no conflict of interest in this work.

Data availability

Data will be made available on request.

Acknowledgements

The PhD fellowship from China Scholarship Council to H. Li is greatly acknowledged.

References

[1] P.G. de Gennes, Wetting: statics and dynamics, Rev. Mod. Phys. 57 (1985) 827–863, https://doi.org/10.1103/RevModPhys.57.827.
[2] V. Bergeron, D. Bonn, J.Y. Martin, L. Vovelle, Controlling droplet deposition with polymer additives, Nature 405 (2000) 772–775, https://doi.org/10.1038/35015525.
[3] S.J. Weinstein, Coating flows, Annu. Rev. Fluid Mech. 36 (2004) 29–53, https://doi.org/10.1146/annurev.fluid.36.050802.122049.
[4] Z. Du, H. Zhou, X. Yu, Y. Han, Controlling the polarity and viscosity of small molecule ink to suppress the contact line receding and coffee ring effect during inkjet printing, Colloids Surf. A Physicochem. Eng. Asp. 602 (2020) 125111, https://doi.org/10.1016/j.colsurfa.2020.125111.
[5] X. Wang, L. Chen, E. Bonaccurso, Comparison of spontaneous wetting and drop impact dynamics of aqueous surfactant solutions on hydrophobic polypropylene surfaces: scaling of the contact radius, Colloid Polym. Sci. 293 (2015) 257–265, https://doi.org/10.1007/s00396-014-3410-x.
[6] M.A. Fardin, M. Hautefeuille, V. Sharma, Spreading, pinching, and coalescence: the Ohnesorge units, Soft Matter 18 (2022) 3291–3303, https://doi.org/10.1039/D2SM00069E.
[7] M. Andersson Trojer, A. Mohamed, J. Eastoe, A highly hydrophobic anionic surfactant at oil–water, water–polymer and oil–polymer interfaces: implications for spreading coefficients, polymer interactions and microencapsulation via internal phase separation, Colloids Surf. A Physicochem. Eng. Asp. 436 (2013) 1048–1059, https://doi.org/10.1016/j.colsurfa.2013.08.005.
[8] V.M. Samsonov, A.S. Ratnikov, Comparative molecular dynamics study of simple and polymer nanodroplet spreading, Colloids Surf. A Physicochem. Eng. Asp. 298 (2007) 52–57, https://doi.org/10.1016/j.colsurfa.2006.12.015.
[9] J. Du, N.T. Chamakos, A.G. Papathanasiou, Q. Min, Initial spreading dynamics of a liquid droplet: the effects of wettability, liquid properties, and substrate topography, Phys. Fluids 33 (2021) 042118, https://doi.org/10.1063/5.0049409.
[10] D. Chaffart, L.A. Ricardez-Sandoval, A moving front kinetic Monte Carlo approach to model sessile droplet spreading on superhydrophobic surfaces, Chem. Eng. Sci. 280 (2023) 119006, https://doi.org/10.1016/j.ces.2023.119006.
[11] D. Bonn, J. Eggers, J. Indekeu, J. Meunier, E. Rolley, Wetting and spreading, Rev. Mod. Phys. 81 (2009) 739–805, https://doi.org/10.1103/RevModPhys.81.739.
[12] L. Chen, E. Bonaccurso, M.E.R. Shanahan, Inertial to viscoelastic transition in early drop spreading on soft surfaces, Langmuir 29 (2013) 1893–1898, https://doi.org/10.1021/la3046862.
[13] A. Carlson, P. Kim, G. Amberg, H.A. Stone, Short and long time drop dynamics on lubricated substrates, EPL 104 (2013) 34008, https://doi.org/10.1209/0295-5075/104/34008.
[14] P.G. Bange, G. Upadhyay, N.D. Patil, R. Bhardwaj, Isothermal and non-isothermal spreading of a viscous droplet on a solid surface in total wetting condition, Phys. Fluids 34 (2022) 112115, https://doi.org/10.1063/5.0122220.
[15] J.C. Bird, S. Mandre, H.A. Stone, Short-time dynamics of partial wetting, Phys. Rev. Lett. 100 (2008) 234501, https://doi.org/10.1103/PhysRevLett.100.234501.
[16] L.H. Tanner, The spreading of silicone oil drops on horizontal surfaces, J. Phys. D Appl. Phys. 12 (1979) 1473–1484, https://doi.org/10.1088/0022-3727/12/9/009.
[17] S. Saritha, X. Zhang, P. Neogi, Wetting kinetics of films containing nonadsorbing polymers, J. Chem. Phys. 122 (2005) 244711, https://doi.org/10.1063/1.1943427.
[18] C. Lv, P. Hao, X. Zhang, F. He, Drop impact upon superhydrophobic surfaces with regular and hierarchical roughness, Appl. Phys. Lett. 108 (2016) 141602, https://doi.org/10.1063/1.4945662.
[19] P. Muralidhar, E. Bonaccurso, G.K. Auernhammer, H.-J. Butt, Fast dynamic wetting of polymer surfaces by miscible and immiscible liquids, Colloid Polym. Sci. 289 (2011) 1609–1615, https://doi.org/10.1007/s00396-011-2475-z.
[20] L. Baroudi, T. Lee, Effect of interfacial mass transport on inertial spreading of liquid droplets, Phys. Fluids 32 (2020) 032101, https://doi.org/10.1063/1.5135728.
[21] S. Mitra, S.K. Mitra, Understanding the early regime of drop spreading, Langmuir 32 (2016) 8843–8848, https://doi.org/10.1021/acs.langmuir.6b02189.
[22] J.R. Castrejón-Pita, A.A. Castrejón-Pita, S.S. Thete, K. Sambath, I.M. Hutchings, J. Hinch, J.R. Lister, O.A. Basaran, Plethora of transitions during breakup of liquid filaments, Proc. Natl. Acad. Sci. USA 112 (2015) 4582–4587, https://doi.org/10.1073/pnas.1418541112.
[23] J. Dinic, V. Sharma, Power laws dominate shear and extensional rheology response and capillarity-driven pinching dynamics of entangled hydroxyethyl cellulose (HEC) solutions, Macromolecules 53 (2020) 3424–3437, https://doi.org/10.1021/acs.macromol.0c00077.
[24] L. Leger, J.F. Joanny, Liquid spreading, Rep. Prog. Phys. 55 (1992) 431–486, https://doi.org/10.1088/0034-4885/55/4/001.
[25] J. Eggers, Nonlinear dynamics and breakup of free-surface flows, Rev. Mod. Phys. 69 (1997) 865–930, https://doi.org/10.1103/RevModPhys.69.865.
[26] L. Courbin, J.C. Bird, M. Reyssat, H.A. Stone, Dynamics of wetting: from inertial spreading to viscous imbibition, J. Phys. Condens. Matter 21 (2009) 464127, https://doi.org/10.1088/0953-8984/21/46/464127.
[27] J. Magnaudet, M.J. Mercier, Particles, drops, and bubbles moving across sharp interfaces and stratified layers, Annu. Rev. Fluid Mech. 52 (2020) 61–91, https://doi.org/10.1146/annurev-fluid-010719-060139.
[28] L. Chen, E. Bonaccurso, Effects of surface wettability and liquid viscosity on the dynamic wetting of individual drops, Phys. Rev. E. 90 (2014) 022401, https://doi.org/10.1103/PhysRevE.90.022401.
[29] H.P. Kavehpour, Coalescence of drops, Annu. Rev. Fluid Mech. 47 (2015) 245–268.
[30] J. Eggers, J.R. Lister, H.A. Stone, Coalescence of liquid drops, J. Fluid Mech. 401 (1999) 293–310, https://doi.org/10.1017/S002211209900662X.
[31] J.D. Paulsen, J.C. Burton, S.R. Nagel, Viscous to inertial crossover in liquid drop coalescence, Phys. Rev. Lett. 106 (2011) 114501, https://doi.org/10.1103/PhysRevLett.106.114501.
[32] Y. Zhu, G. Kong, C. Che, Thermally-induced self-cutting surfaced reduced graphene oxide fibers for smart fire alarm, Colloids Surf. A Physicochem. Eng. Asp. 675 (2023) 132032, https://doi.org/10.1016/j.colsurfa.2023.132032.
[33] A.P. Terzyk, The influence of activated carbon surface chemical composition on the adsorption of acetaminophen (paracetamol) in vitro Part II. TG, FTIR, and XPS analysis of carbons and the temperature dependence of adsorption kinetics at the neutral pH, Colloids Surf. A Physicochem. Eng. Asp. 177 (2001) 23–45.
[34] F. Torrisi, T. Hasan, W. Wu, Z. Sun, A. Lombardo, T.S. Kulmala, G.-W. Hsieh, S. Jung, F. Bonaccorso, P.J. Paul, D. Chu, A.C. Ferrari, Inkjet-printed Graphene electronics, ACS Nano 6 (2012) 2992–3006, https://doi.org/10.1021/nn2044609.
[35] M. Vaseem, G. McKerricher, A. Shamim, Robust design of a particle-free silver-organo-complex ink with high conductivity and inkjet stability for flexible electronics, ACS Appl. Mater. Interfaces 8 (2016) 177–186, https://doi.org/10.1021/acsami.5b08125.
[36] Q. Zhang, X. Jiang, D. Brunello, T. Fu, C. Zhu, Y. Ma, H.Z. Li, Initial coalescence of a drop at a planar liquid surface, Phys. Rev. E 100 (2019) 033112, https://doi.org/10.1103/PhysRevE.100.033112.
[37] C. Vallés, Rheology of graphene oxide dispersions, Graph. Oxide (2016) 121–146, https://doi.org/10.1002/9781119069447.ch4.
[38] C. Vallés, R.J. Young, D.J. Lomax, I.A. Kinloch, The rheological behaviour of concentrated dispersions of graphene oxide, J. Mater. Sci. 49 (2014) 6311–6320.
[39] P. Kumar, U.N. Maiti, K.E. Lee, S.O. Kim, Rheological properties of graphene oxide liquid crystal, Carbon 80 (2014) 453–461.
[40] R.B. Bird, R.C. Armstrong, O. Hassager, Dynamics of polymeric liquids. Fluid Mechanics, 1, John Wiley & Sons, Inc, New York, 1987.
[41] R. Lapasin, S. Pricl, Rheology of Industrial Polysaccharides: Theory and Applications, Chapman and Hall, London, 1995.